

**Prediction of Improved Thermoelectric Performance by
Ordering in Double Half-Heusler Materials**

Journal:	<i>Journal of Materials Chemistry A</i>
Manuscript ID	TA-ART-08-2020-008364.R2
Article Type:	Paper
Date Submitted by the Author:	13-Oct-2020
Complete List of Authors:	Guo, Shuping; Institute of Solid State Physics Chinese Academy of Sciences, Key Laboratory of Materials Physics Liu, Zihang; National Institute for Materials Science, Feng, Zhenzhen; Henan University, Institute for Computational Materials Science, School of Physics and Electronics Jia, Tiantian; Institute of Solid State Physics, Chinese Academy of Sciences, Anand, Shashwat; Northwestern University, Materials Science and Engineering Snyder, G.; Northwestern University, Materials Science Zhang, Yongsheng; Institute of Solid State Physics, Chinese Academy of Sciences,

ARTICLE TYPE

Cite this: DOI: 10.1039/xxxxxxxxxx

Prediction of Improved Thermoelectric Performance by Ordering in Double Half-Heusler Materials †

Shuping Guo,^{abd} Zihang Liu,^c Zhenzhen Feng,^e Tiantian Jia,^{ad} Shashwat Anand,^b G. Jeffrey Snyder^{*b} and Yongsheng Zhang^{*ad}

Received Date

Accepted Date

DOI: 10.1039/xxxxxxxxxx

www.rsc.org/journalname

Many Cobalt (Co)-based 18-electron half-Heusler compounds usually exhibit good thermoelectric properties. Due to the increasing scarcity of the Co, replacing Co with Fe and Ni to form double half-Heusler compound is an effective way to form stable nominal 18-electron ground states and eliminate the need for Co. We investigate here the phase stability of three double half-Heusler systems (TiFe_{1-x}Ni_xSb, ZrFe_{1-x}Ni_xBi and VFe_{1-x}Ni_xGe) through density-functional theory combined with cluster expansion method. Two stable ground state ordered structures (Ti₄Fe₂Ni₂Sb₄ and V₄Fe₂Ni₂Ge₄) are identified. Based on the calculations of electronic and phonon structures, we find that the two ordered structures can maintain the excellent electrical properties of pristine half-Heusler compounds but with low thermal conductivity as found experimentally. The p-type (n-type) zT values of Ti₄Fe₂Ni₂Sb₄ and V₄Fe₂Ni₂Ge₄ are predicted to reach to 1.75 (0.64) and 1.33 (0.95), respectively. Our work not only provides promising double half-Heusler candidates for further experimental investigation but also suggests that forming ordered structure instead of solid solution is an efficient way to achieve excellent thermoelectric properties in the double half-Heusler systems.

1 Introduction

Thermoelectric materials have long been used in various practical waste heat recovery systems because of the merit of simple and environmentally friendly operation.¹ It requires a high value of dimensionless thermoelectric figure of merit (zT) to reach the high energy conversion efficiency, $zT = S^2\sigma T / (\kappa_e + \kappa_l)$, where S is the Seebeck coefficient, σ the electrical conductivity, κ_e the electronic thermal conductivity and κ_l the dominating lattice contributions of thermal conductivity.² The zT values of various thermoelectric materials have been undergone a progressive increment thanks to the advances in synthesis techniques and computational methods.³ The peak zT for a given semiconductor is determined by the thermoelectric quality factor⁴ where the electronic contribution is determined by the weighted mobility⁵.

Among them, half-Heusler (HH) compounds are considered as one of the best high-temperature thermoelectric materials owing to the intrinsically high weighted mobility, low cost, robust thermal and mechanical stability.^{6,7} However, its lattice thermal conductivity is so high ($> 15 \text{ W m}^{-1} \text{ K}^{-1}$) that impedes the thermoelectric applications⁸.

ABC Half-Heusler compounds compose of four face-centered cubic (fcc) sublattices with A, B and C atoms occupying at the (0, 0, 0), (0.25, 0.25, 0.25) and (0.5, 0.5, 0.5) positions as well as one vacant fcc sublattice⁹, shown in Fig. 1. Stable semiconducting HH compounds generally follow a valence balanced rule¹⁰. When B is a transition metal, it becomes the well known 18 valence electron counting (VEC) rule: 18 valence electrons fill all bonding states (the valence band), while leave all antibonding states (the conduction band) empty.^{9,10} In other words, the Fermi energy level is right inside the band gap. Such HH compounds are particularly stable and exhibit semiconducting properties suitable for thermoelectric applications. However, the number of 18-electron HH compounds is rare¹¹. In addition to the 18-electron HH compounds, there are many 17- or 19-electron HH: the Fermi level shifts into the valence band or conduction band, respectively. Thus, the corresponding HH compounds turn into metals and the partially occupied bonding or anti-bonding states weaken the bonding interactions.⁹ Therefore, based on the 18-electron rule, mixing 17- and 19-electron HH systems can form nominally 18-

^aKey Laboratory of Materials Physics, Institute of Solid State Physics, HFIPS, Chinese Academy of Sciences, Hefei 230031, China. E-mail: yshzhang@theory.issp.ac.cn

^bDepartment of Materials Science and Engineering, Northwestern University, Evanston, IL 60208, USA. E-mail: jeff.snyder@northwestern.edu

^cWPI Center for Materials Nanoarchitectonics (WPI-MANA), National Institute for Materials Science (NIMS), Namiki 1-1, Tsukuba 305-0044, Japan.

^dScience Island Branch of Graduate School, University of Science and Technology of China, Hefei 230026, China.

^eInstitute for Computational Materials Science, School of Physics and Electronics, Henan University, Kaifeng 475004, China.

†Electronic Supplementary Information (ESI) available: All the cross validation scores (CVs) and effective cluster interactions (ECIs). See DOI: 00.0000/00000000.

electron double half-Heusler compounds, which provides a huge composition space to search novel thermoelectric materials¹². Moreover, the mixture could scatter phonons efficiently, reducing the lattice thermal conductivity and improving the thermoelectric performance. Using such ideas, Tobola et al. found that a stable 17-19 electron $\text{TiFe}_{0.5}\text{Ni}_{0.5}\text{Sb}$ solid solution exhibits semiconducting properties by substituting Co by Fe and Ni in TiCoSb .¹³ Recently, Liu et al. synthesized the $\text{TiFe}_{0.5}\text{Ni}_{0.5}\text{Sb}$ sample and measured a reduced thermal conductivity of $7.3 \text{ W m}^{-1} \text{ K}^{-1}$ at 300 K.¹⁴ Anand et al. predicted over 100 new double half-Heuslers to be stable and calculated relatively low thermal conductivities ($< 20 \text{ W m}^{-1} \text{ K}^{-1}$ at 300 K) for 18 examples¹².

Cobalt-based HH materials have been attracting increasing attention because of the large p-type band degeneracy¹⁵ which leads to high weighted mobility. Still, the intrinsically high thermal conductivity of pristine compounds largely impedes the large-scale application. Alloying to form a solid solution^{16–18} successfully improves the thermoelectric performance, e.g. the p-type zT values of $\text{Ti}_{0.8}\text{Hf}_{0.2}\text{Fe}_{0.4}\text{Ni}_{0.6}\text{Sb}$ and $\text{ZrCoBi}_{0.65}\text{Sb}_{0.15}\text{Sn}_{0.2}$ reach 1.4¹⁴ and 1.4¹⁹ at high temperature, respectively. Besides, our recent high-throughput computational work reported another Co-based HH compound (VCoGe) is also a promising thermoelectric candidate with p-type electrical properties conducive to high zT ^{20,21}. However, Co is frequently used in catalysts, lithium-ion batteries as well as superalloys. Given the limited global supply of Co, it can quickly become scarce. As a consequence, substituting Fe (17-electron) and Ni (19-electron) for Co in the three Co-based systems (TiCoSb , ZrCoBi and VCoGe) would lead to the exciting discovery of novel 18-electron candidates with earth-abundant elements.

The mixture of two phases could form the solid solution at high temperature and ordered structure at low temperature. Alloying to form solid solution at high temperature has long been used to decrease the thermal conductivity but it may deteriorate the carrier mobility. In contrast, an ordered structure with low thermal conductivity could maintain the high weighted mobility²². Several high-throughput works indicated that the electronic structure determines the good thermoelectric performance of half-Heusler compounds.^{7,20} Therefore, it is desirable to discover ordered structures with better thermoelectric properties than solid solutions in Co-based HH compounds. The ordered, stable structures in the double HH systems have not been studied experimentally. Theoretical prediction of the structures and analysis of their thermoelectric properties will greatly speed the search for new materials.

In this work, substituting Co with its neighboring elements (Fe and Ni) in the three Co-based HH compounds (TiCoSb , ZrCoBi and VCoGe), we predict the phase stability and possible stable ordered ground state structures in the three pseudo-binary 17-19 electron mixtures of $\text{TiFe}_{1-x}\text{Ni}_x\text{Sb}$, $\text{ZrFe}_{1-x}\text{Ni}_x\text{Bi}$ and $\text{VFe}_{1-x}\text{Ni}_x\text{Ge}$ systems through the cluster expansion (CE) method. It is noteworthy that only $\text{TiFe}_{1-x}\text{Ni}_x\text{Sb}$ and $\text{VFe}_{1-x}\text{Ni}_x\text{Ge}$ possess the stable ground state structures at $x = 0.5$ ($\text{Ti}_4\text{Fe}_2\text{Ni}_2\text{Sb}_4$ and $\text{V}_4\text{Fe}_2\text{Ni}_2\text{Ge}_4$). Since random solid solutions are found experimentally and $x \neq 0.5$ compositions can be used to tune the thermoelectric properties¹², we simulate the solid solution using

the special quasi-random structure (SQS). It turns out that for the $\text{TiFe}_{1-x}\text{Ni}_x\text{Sb}$ and $\text{VFe}_{1-x}\text{Ni}_x\text{Ge}$ systems, the ordered structures ($\text{Ti}_4\text{Fe}_2\text{Ni}_2\text{Sb}_4$ and $\text{V}_4\text{Fe}_2\text{Ni}_2\text{Ge}_4$) have potentially higher weighted mobility than those of the corresponding solid solution ($\text{Ti}_{16}\text{Fe}_8\text{Ni}_8\text{Sb}_{16}$ and $\text{V}_{16}\text{Fe}_8\text{Ni}_8\text{Ge}_{16}$). Additionally, even though the thermal conductivity of the ordered $\text{V}_4\text{Fe}_2\text{Ni}_2\text{Ge}$ structure is higher than that of the solid solution, the difference is becoming smaller with increasing temperature. The low thermal conductivity ($3.6 \text{ W m}^{-1} \text{ K}^{-1}$ at 1000 K) of $\text{Ti}_4\text{Fe}_2\text{Ni}_2\text{Sb}_4$ comes from depressed acoustic branches and then low phonon velocities. Balancing the electrical and thermal contributions, $\text{Ti}_4\text{Fe}_2\text{Ni}_2\text{Sb}_4$ and $\text{V}_4\text{Fe}_2\text{Ni}_2\text{Ge}_4$ are predicted to have high p-type zT values (1.75 and 1.33) at high temperature. Our work suggests that alloying 17- and 19-electron half-Heusler is a feasible way to find novel ordered compounds with high weighted mobility and power factor as well as low thermal conductivity, providing insights into optimizing and designing promising thermoelectric half-Heusler compounds.

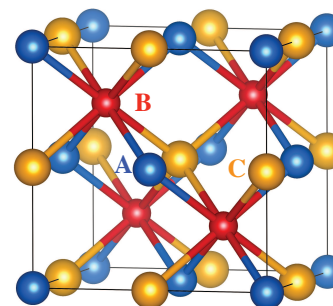


Fig. 1 Crystal structure of the half-Heusler ABC compound. The blue, red and yellow spheres represent the A, B and C atoms, respectively.

2 Methodology

2.1 Density Functional Theory

Using Vienna Ab Initio Simulation Package (VASP), first-principles density functional theory (DFT) calculations are performed with projector augmented wave (PAW)²³ scheme. The electronic exchange correlation functional use the Perdew, Burke, and Ernzerhof (PBE) formulation under a gradient-generalized approximation (GGA)²⁴. We use a constant energy cutoff of 500 eV to truncate the plane-wave basis and a roughly constant density of k-points (30 \AA^3) of Monkhorst-Pack²⁵ point meshes to sample the Brillouin zones. All structures are relaxed with respect to all the forces and components of the tensors are below 0.01 eV/Å and 0.2 kbar, respectively. To compare the band structures of ground states and solid solutions, we use a band unfolding method (BandUP code)²⁶ to unfold the band structure of a supercell into its primitive Brillouin zone.

2.2 Cluster Expansion

To predict the novel crystal structures of HH compounds, we use a cluster expansion formalism^{27–29} to obtain the phase diagram of the pseudo-binary A_{1-x}B_x as a function of doping concentration (x) of B in the half-Heusler structure. Cluster expansion method relies on the use of occupation variables assigned to each site i

that is 1 if it is occupied and 0 if it vacant. The formation energy (E_f) is defined as,

$$E_f = [E(\phi) - (1-x)E(A) - xE(B)]/N_{mix} \quad (1)$$

where $E(\phi)$, $E(A)$ and $E(B)$ are the total energies of A-B mixing configuration (ϕ), and pristine compositions of A and B, respectively. And x is the mixing constituent of B atoms and N_{mix} is the number of mixing atoms. In analogy to a generalized Ising model, the formation energy (E_f) of any arbitrary atomic configuration then can be uniquely determined as a series expansion of basic functions which go over all possible clusters in the lattice:

$$E_f(\phi) = J_0 + \sum_i J_i \phi_i + \frac{1}{2!} \sum_{i \neq j} J_{i,j} \phi_i \phi_j + \frac{1}{3!} \sum_{i \neq j \neq k} J_{i,j,k} \phi_i \phi_j \phi_k + \dots \quad (2)$$

where the coefficients $J_{i,j,k,\dots}$ are the effective cluster interactions (ECIs) related to a cluster of lattice sites (i, j, k, \dots). This sum converges rapidly and in most cases the formation energy can be described with only a few pairs as well as the multi-site interactions of short range.³⁰ The cross-validation (CV) score is used to evaluate the predictive power of one group of ECIs and then decide the optimal one. After fitting 80 ordered configurations, the CVs of our three systems decrease to below 30 meV/mixing atom. The convex hull (or the ground state line) is identified with no new structures below the line. The detailed CV and ECIs are listed in Table S1 in the Supporting Information. The cluster expansion calculations are performed using the Alloy Theoretic Automated Toolkit (ATAT)³¹.

2.3 Special quasi-random structure (SQS) approach

Because solid solutions are important to optimize the thermoelectric properties, we need to consider such phases in our calculations.¹³ To mimic the random occupancy of atom in solid solutions (disorder), we need to construct large supercells, which are accompanied by the prohibitive computational cost. Special quasi-random structures (SQS) can overcome this limitation. All configurations are specially designed within a small periodic structure with a few atoms (2-16). The pair and multisite correlation functions of each configuration are calculated, and the best SQS structure is chosen with the correlation functions close to the ideal disordered system. This method has successfully used to describe the solid solution of SrTi_{1-x}Nb_xO₃³², rocksalt IV-VI semiconductors³³, as well as half-Heusler systems^{18,34}. Because Fe and Ni are alloyed at one of the fcc sublattice, we take the SQS structures predicted by Wolverton³⁵ to study the thermoelectric properties of the solid solutions.

2.4 Thermoelectric properties

The electrical (S and σ) and thermal (κ) transport properties are important to determine the thermoelectric performance. From the thermoelectric equations³⁶, the effective masses are key parameters to characterize the electrical transport properties. Based on the rigid band approximation, the density of states (DOS) effective mass (m_d^*) is calculated through fitting the DOS around

the Fermi level

$$DOS(E) = \frac{1}{2\pi^2} \left(\frac{2m_d^*}{\hbar^2} \right)^{3/2} E^{1/2} \quad (3)$$

The band effective mass (m_b^*) is extracted from the band structure, $m_b^* = (m_1^* m_2^* m_3^*)^{1/3}$, where m_1^* , m_2^* and m_3^* are the effective masses along the x , y and z directions, respectively. The Seebeck coefficient (S) and electrical conductivity (σ) are calculated by solving the Boltzmann transport equations (BTE) under the constant relaxation time approximation (CRTA, $\tau_{ch} = 10^{-14}$ fs) as implemented in the BoltzTraP code^{37,38}. The CRTA has been widely used in thermoelectric material simulations and generates reasonable results³⁹. To valid the constant relaxation time approximation, we use the deformation potential theory to calculate the electronic relaxation times of a ground state structure (V₄Fe₂Ni₂Ge₄, Fig. S2 in Supplementary Information). We notice that the electron relaxation time is around 10 fs, which is close to the constant relaxation time (10 fs). Therefore, it is reasonable and convenient to use the constant relaxation time approximation to evaluate the electrical properties. We use a high density of k points (60 Å³) to obtain the accurate electrical transport properties.

Since the thermal transport depends on the phonon properties, we calculate the phonon dispersions within a 2×2×2 supercells with 96 atoms using the finite displacement method implemented in Phonopy⁴⁰ package. To determine the amplitudes of the three-phonon processes, the third-order interatomic force constants (ICFs) are obtained by the thirdorder.py code⁴¹. The third coordination shell is considered for the interatomic interactions. The lattice thermal conductivity is attained by solving the full linearized phonon BTE with a (6×6×6) grid as implemented in the almaBTE code.⁴² To consider the dipole-dipole interactions, the Born effective charges and dielectric tensors are calculated through VASP.

3 Results and discussion

3.1 Phase diagrams and crystal structures of TiFe_{1-x}Ni_xSb, ZrFe_{1-x}Ni_xBi and VFe_{1-x}Ni_xGe systems

Mixing 17- and 19-electron HH compounds could form the stable double HH ordered structures¹². To search for the stable ordered structures in the three kinds of pseudo-binary mixtures (TiFe_{1-x}Ni_xSb, ZrFe_{1-x}Ni_xBi and VFe_{1-x}Ni_xGe), we perform the cluster expansion (CE) method to construct the mixing phase diagrams (Fig. 2), which needs to fit the ECIs using the DFT calculated energies of many configurations (green crosses in Fig. 2). If the end points are 17-electron (TiFeSb, ZrFeBi and VFeGe) and 19-electron (TiNiSb, ZrNiBi, and VNiGe) compounds, we find that all the formation energies are negative, indicating all mixtures are stable relative to their corresponding two end points. The pseudo-binary convex hull (the ground state line, black dotted lines in Fig. 2) is constructed by connecting the vertices, and the stable ground structures are identified (the red empty circles in Fig. 2). However, nominally 17- and 19-electron HH compositions are well known to be thermodynamically unstable and usually phase separate into off-stoichiometric defective HH phases^{11,43,44}. Based on the phase diagrams from Open

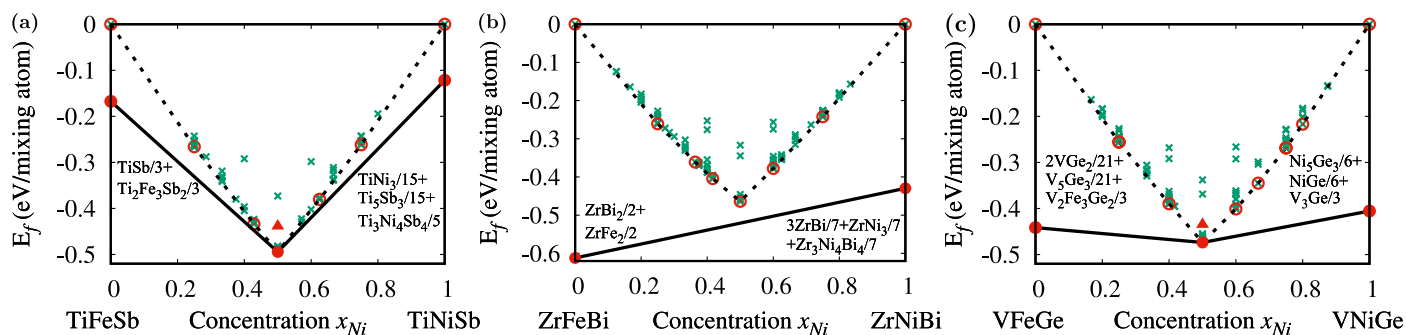


Fig. 2 DFT+CE predicted ground state lines of the (a) $\text{TiFe}_{1-x}\text{Ni}_x\text{Sb}$, (b) $\text{ZrFe}_{1-x}\text{Ni}_x\text{Bi}$ and (c) $\text{VFe}_{1-x}\text{Ni}_x\text{Ge}$ systems. The green crosses mean the formation energies calculated by DFT. The black lines with red solid circles are the ground state lines after considering the phase separation. The red triangles represent the SQS structures ($\text{Ti}_{16}\text{Fe}_8\text{Ni}_8\text{Sb}_{16}$ and $\text{V}_{16}\text{Fe}_8\text{Ni}_8\text{Ge}_{16}$). There are two stable ground states ($\text{Ti}_4\text{Fe}_2\text{Ni}_2\text{Sb}_4$ and $\text{V}_4\text{Fe}_2\text{Ni}_2\text{Ge}_4$) with lower formation energy compared to that of corresponding SQS structures.

Quantum Materials database^{45,46}, the 17- and 19-electron HH compounds will thermodynamically decompose into corresponding relative compounds: TiFeSb , TiNiSb , ZrFeBi , ZrNiBi , VFeGe and VNiGe divide into $(\text{TiSb}/3 + \text{Ti}_2\text{Fe}_3\text{Sb}_2/3)$, $(\text{TiNi}_3/15 + \text{Ti}_3\text{Ni}_4\text{Sb}_4/15 + \text{Ti}_5\text{Sb}_3/5)$, $(\text{ZrBi}_2/2 + \text{ZrFe}_2/2)$, $(3\text{ZrBi}/7 + \text{ZrNi}_3/7 + \text{Zr}_3\text{Ni}_4\text{Bi}_4/7)$, $(2\text{VGe}_2/21 + \text{V}_5\text{Ge}_3/21 + \text{V}_2\text{Fe}_3\text{Ge}_2/3)$ and $(\text{Ni}_5\text{Ge}_3/6 + \text{NiGe}/6 + \text{V}_3\text{Ge}/3)$, respectively. The total energies of all these decomposed compounds are calculated using DFT, and we find that the formation energies of these decomposed mixtures are 0.17, 0.12, 0.61, 0.43, 0.44 and 0.41 eV/mixing atom lower than those of the corresponding 17- and 19-electron HH compounds, respectively. Since there are lower energies for those end point HH compositions, we have to replot the convex hulls in three phase diagrams (the black lines in Fig. 2). It turns out that only $\text{Ti}_4\text{Fe}_2\text{Ni}_2\text{Sb}_4$ and $\text{V}_4\text{Fe}_2\text{Ni}_2\text{Ge}_4$ are the thermodynamically stable mixtures, and their formation energies are -0.49 and -0.47 eV/mixing atom, respectively. The predicted crystal structures of the $\text{ZrFe}_{1-x}\text{Ni}_x\text{Bi}$ system are all above the new convex hull, indicating the thermodynamically unstable. For the two stable compounds ($\text{Ti}_4\text{Fe}_2\text{Ni}_2\text{Sb}_4$ and $\text{V}_4\text{Fe}_2\text{Ni}_2\text{Ge}_4$), the mixing ratio of 17- and 19-electron HH compounds is 1:1. This means that one conduction band electron in the 19-electron HH compound will fill the one valence band hole in the 17-electron HH compound, which makes the double HH mixture semiconductor. Taking $\text{Ti}_4\text{Fe}_2\text{Ni}_2\text{Sb}_4$ (Fig. 3a) as an example, the unfolded band structures show that the Fermi level is in the band gap, exhibiting the semiconducting properties (Fig. 4). This verifies the significance of the 18-electron criteria for half-Heusler thermoelectric materials.

The theoretically predicted $\text{Ti}_4\text{Fe}_2\text{Ni}_2\text{Sb}_4$ and $\text{V}_4\text{Fe}_2\text{Ni}_2\text{Ge}_4$ crystal structures (Table 1) have the same space group ($I\bar{4}2d$). However, the corresponding SQS structure has the space group of P1. Therefore, we investigate how the (dis)order behavior affects the structural features. In the ordered ground state crystal structures of $\text{Ti}_4\text{Fe}_2\text{Ni}_2\text{Sb}_4$, the Ti and Sb atoms reside on the tetrahedral sites and form the octahedrons. Fe (or Ni) atoms fill the octahedral center, leading to the interatomic distances $d_{\text{Fe-Sb}} = d_{\text{Fe-Ti}} = d_{\text{Ni-Ti}} = d_{\text{Ni-Sb}} = 2.567 \text{ \AA}$. The bonding between Ti and Sb atoms is $d_{\text{Ti-Sb}} = 2.963 \text{ \AA}$. There is only one kind of bond length (fixed) for any two elements in the high-symmetry ordered

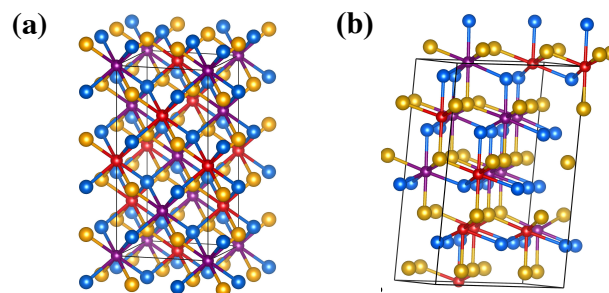


Fig. 3 Crystal structures of (a) the theoretically predicted ground state structures of $\text{Ti}_4\text{Fe}_2\text{Ni}_2\text{Sb}_4$ ($\text{V}_4\text{Fe}_2\text{Ni}_2\text{Ge}_4$) and (b) SQS structure $\text{Ti}_{16}\text{Fe}_8\text{Ni}_8\text{Sb}_{16}$ ($\text{V}_{16}\text{Fe}_8\text{Ni}_8\text{Ge}_{16}$). The blue, red, purple and yellow spheres represent the Ti, Fe, Ni and Sb atoms, respectively.

$\text{Ti}_4\text{Fe}_2\text{Ni}_2\text{Sb}_4$, (e.g. $d_{\text{Fe-Sb}} = 2.567 \text{ \AA}$), indicating no bond diversity⁴⁷. However, in the $\text{Ti}_{16}\text{Fe}_8\text{Ni}_8\text{Sb}_{16}$ SQS structure, the low symmetry operation leads to a larger bond length variety: each Fe (Ni) atom is eight coordinated by four Ti and four Sb with the bond length of 2.38-2.58 (2.54-2.63) and 2.51-2.59 (2.55-2.61) \AA , respectively. The theoretically predicted crystal structures of $\text{VFe}_{1-x}\text{Ni}_x\text{Ge}$ system ($\text{V}_4\text{Fe}_2\text{Ni}_2\text{Ge}_4$ and $\text{V}_{16}\text{Fe}_8\text{Ni}_8\text{Ge}_{16}$) are shown in the Supporting Information (Fig. S1). The atomic positions of disordered SQS structures ($\text{Ti}_{16}\text{Fe}_8\text{Ni}_8\text{Sb}_{16}$ and $\text{V}_{16}\text{Fe}_8\text{Ni}_8\text{Ge}_{16}$) are tabulated in the Supporting Information (Table S2) as well.

Knowledge of the composition phase stability is essential to engineer desirable properties such as dopability, electronic structure, alloying, and microstructure design using phase boundary mapping. The ground state structures undergo an order-disorder transition with increasing temperature. From experimental observations, such mixtures could form the solid solutions by annealing the samples from high temperature ($> 1000 \text{ K}$).¹³ Therefore, the stability behaviors of the solid solutions should be considered as well. For the two systems with stable ground state structures ($\text{Ti}_4\text{Fe}_2\text{Ni}_2\text{Sb}_4$ and $\text{V}_4\text{Fe}_2\text{Ni}_2\text{Ge}_4$), we calculate the formation energies of the corresponding SQS structures ($x = 0.5$: $\text{Ti}_{16}\text{Fe}_8\text{Ni}_8\text{Sb}_{16}$ and $\text{V}_{16}\text{Fe}_8\text{Ni}_8\text{Ge}_{16}$) (red upward triangles in Fig. 2) representing the solid solutions. Clearly, we see that the formation energies of $\text{Ti}_{16}\text{Fe}_8\text{Ni}_8\text{Sb}_{16}$ and $\text{V}_{16}\text{Fe}_8\text{Ni}_8\text{Ge}_{16}$ SQS structures are 0.05 and 0.03 eV/mixing-atom higher than those of the

Table 1 DFT+CE predicted ground state structures (space group: $I\bar{4}2d$) of $Ti_4Fe_2Ni_2Sb_4$ ($a = b = 5.928 \text{ \AA}$, $c = 11.855 \text{ \AA}$) and $V_4Fe_2Ni_2Ge_4$ ($a = b = 5.545 \text{ \AA}$, $c = 11.090 \text{ \AA}$).

System	Atom		x	y	z
$Ti_4Fe_2Ni_2Sb_4$	Ti	4d	-0.250	0.250	0.125
	Fe	2b	0.000	0.000	0.500
	Ni	2a	0.000	0.000	0.000
	Sb	4d	0.250	0.250	0.125
$V_4Fe_2Ni_2Ge_4$	V	4d	-0.250	0.250	0.125
	Fe	2b	0.000	0.000	0.500
	Ni	2a	0.000	0.000	0.000
	Ge	4d	0.250	0.250	0.125

$Ti_4Fe_2Ni_2Sb_4$ and $V_4Fe_2Ni_2Ge_4$ ordered structures, respectively. The small energy differences between the SQS and the ordered structures suggest that the solid solution is a metastable phase, and it might be formed at high temperature when the configurational entropy plays an important role. The energy difference between solid solution and ordered phase is not big (~ 0.05 eV/mixing atom), which would like to form short range order in the real materials. This is consistent with the experimentally observed short order behavior in the ternary defective half-Heusler phases.⁴⁸ The energy differences of these two systems can be overcome at 575 and 348 K by thermal energy ($k_B T$) alone. These temperatures could be used as roughly estimated for the order-disorder phase transitions temperatures. Therefore, long-time annealing at relatively low temperature (e.g. 500-600 K) could potentially stabilize the ordered double half-Heusler structure.

3.2 Thermoelectric properties of $TiFe_{1-x}Ni_xSb$ and $VFe_{1-x}Ni_xGe$ systems

3.2.1 Electronic structures

The electrical properties (S and σ) strongly depend on the electronic structures, such as the effective masses, the band degeneracy (N_v), etc. The structures of the theoretically predicted ordered ground state structures ($Ti_4Fe_2Ni_2Sb_4$ and $V_4Fe_2Ni_2Ge_4$, in Fig. 3) and their corresponding SQS structures are constructed based on the primitive cell of the HH structure. In principle, the number of bands and the first Brillouin zones of these structures are significantly different. Therefore, to compare the electronic structures and properties of these structures, we unfold their electronic band structures along the high symmetry directions of the pristine half-Heusler structure, given in Fig. 4.

As can be expected from the VEC of 18, these compounds (the ordered $Ti_4Fe_2Ni_2Sb_4$, $V_4Fe_2Ni_2Ge_4$; and the disordered $Ti_{16}Fe_8Ni_8Sb_{16}$, $V_{16}Fe_8Ni_8Ge_{16}$ SQS structures) are all semiconductors with the indirect band gaps of 0.63, 0.51, 0.44 and 0.38 eV, respectively. Additionally, we note the favorable band structure features for high thermoelectric performance, such as large valence band degeneracy. The valence band maximum (VBM) and second VBM (VBM-2) locate at the L and Γ points with the

band degeneracy of 8 (N_v^L) and 3 (N_v^Γ), respectively. For the $TiFe_{0.5}Ni_{0.5}Sb$ systems (Fig. 4a and 4b), since the energy difference between VBM and VBM-2 is pretty small (< 0.2 eV), the band degeneracy of the valence band can be added up to $N_v = 11$. Moreover, $Ti_{16}Fe_8Ni_8Sb_{16}$ -SQS has a flat band at VBM along the direction $L \rightarrow \Gamma$, indicating large valence DOS effective but low carrier mobility. The conduction band maximum (CBM) of the four compounds are at the X point with the band degeneracy of $N_c^X = 3$. In addition, $V_4Fe_2Ni_2Ge_4$ has a secondary CBM at the K point ($N_c^K = 3$). The ordered structures all have an extra VBM (like Γ -X for $Ti_4Fe_2Ni_2Sb_4$) or CBM (like K- Γ for $Ti_4Fe_2Ni_2Sb_4$), compared to the disordered phases ($Ti_{16}Fe_8Ni_8Sb_{16}$, $V_{16}Fe_8Ni_8Ge_{16}$). Additionally, the larger band gaps in the ordered structures could suppresses the possible bipolar effect. Therefore, the ground state structures would have better electrical properties than the SQS structures.

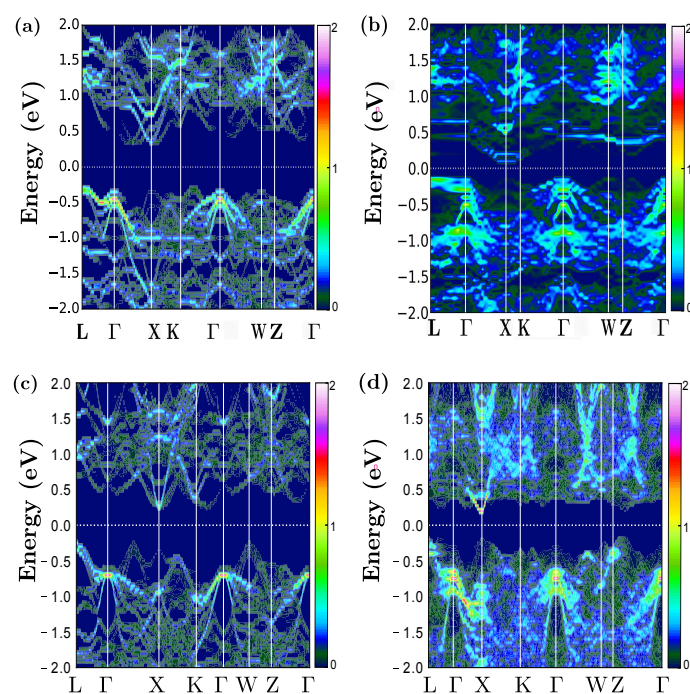


Fig. 4 Unfolded electronic band structures of (a) $Ti_4Fe_2Ni_2Sb_4$, (b) SQS structure $Ti_{16}Fe_8Ni_8Sb_{16}$, (c) $V_4Fe_2Ni_2Ge_4$ and (d) SQS structure $V_{16}Fe_8Ni_8Ge_{16}$. The scale bar in (a), (b), (c) and (d) is the magnitude of the spectral weight, which characterize the probability of the primitive cell eigenstates contributing to a particular supercell eigenstate of the same energy.

3.2.2 Electrical transport properties

After investigating the electronic structures of these compounds, we further exploit their transport properties. Using the rigid band approximation (RBA) and the semiclassical Boltzmann transport theory with the constant relaxation time approximation and the same relaxation time for all structures ($\tau_{ch} = 10$ fs), we calculate the electrical transport properties of ground state structures ($Ti_4Fe_2Ni_2Sb_4$, $V_4Fe_2Ni_2Ge_4$) and SQS structures ($Ti_{16}Fe_8Ni_8Sb_{16}$, $V_{16}Fe_8Ni_8Ge_{16}$). From the experimental measurements¹⁴, the carrier concentrations of p- ($TiFe_{0.4}Ni_{0.6}Sb$) and n-type ($TiFe_{0.6}Ni_{0.4}Sb$) samples $TiFe_{0.5}Ni_{0.5}Sb$ are 6×10^{21}

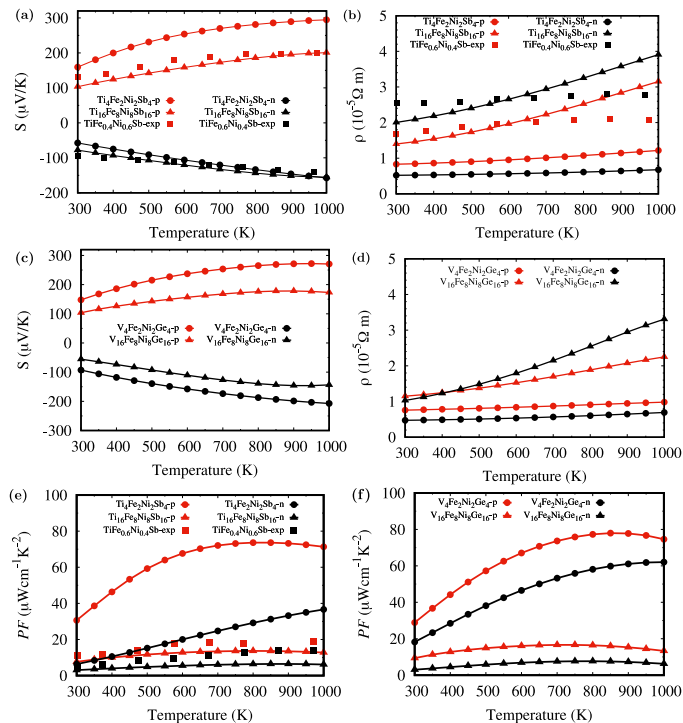


Fig. 5 Temperature dependent (a) (c) Seebeck coefficients, (b) (d) electrical resistivities and (e) (f) power factors (at the same $\tau_{ch} = 10$ fs and carrier concentration of 10^{21} cm^{-3}) of the ordered ($\text{Ti}_4\text{Fe}_2\text{Ni}_2\text{Sb}_4$ and $\text{V}_4\text{Fe}_2\text{Ni}_2\text{Ge}_4$, line with circles) and SQS ($\text{Ti}_{16}\text{Fe}_8\text{Ni}_8\text{Sb}_{16}$ and $\text{V}_{16}\text{Fe}_8\text{Ni}_8\text{Ge}_{16}$, line with triangles) structures. The squares are experimental data from Ref. [14]. The red and black lines represent the p- and n-type, respectively.

cm^{-3} and $4.85 \times 10^{21} \text{ cm}^{-3}$. The figures of power factor versus carrier concentration of ordered ground states ($\text{Ti}_4\text{Fe}_2\text{Ni}_2\text{Sb}_4$ and $\text{V}_4\text{Fe}_2\text{Ni}_2\text{Ge}_4$) and SQS structures ($\text{Ti}_{16}\text{Fe}_8\text{Ni}_8\text{Sb}_{16}$ and $\text{V}_{16}\text{Fe}_8\text{Ni}_8\text{Ge}_{16}$) are shown in Fig. S3 in the Supplementary Information. We find that the carrier concentrations corresponding to the maximum power factors are slightly higher than 10^{21} cm^{-3} . This is in a reasonable agreement with the experimentally suggested concentration (10^{21} cm^{-3}). Therefore, we take the carrier concentration (n) of 10^{21} cm^{-3} , to calculate the temperature-dependent Seebeck coefficients and electrical resistivities of the ordered $\text{Ti}_4\text{Fe}_2\text{Ni}_2\text{Sb}_4$ and $\text{Ti}_{16}\text{Fe}_8\text{Ni}_8\text{Sb}_{16}$ -SQS (Fig. 5a and 5b) structures and compare the theoretical results with the experimental measurements. The experimental results of Seebeck coefficients and electrical resistivities are in agreement with our SQS results, suggesting the constant relaxation time approximation and $\tau_{ch} = 10$ fs for the SQS is appropriate.

From Fig. 5, we find that the p-type compounds have higher Seebeck coefficients than n-type. Additionally, the Seebeck coefficients of ordered structures are larger than those of the solid solutions. It is well known that high DOS effective mass (m_d^*) leads to the larger Seebeck coefficient at the same charge carrier concentration.⁴⁹ This is illustrated in the Mott equation for the simple metals

$$S = \frac{8\pi^2 k_B^2}{3eh^2} m_d^* T \left(\frac{\pi}{3n} \right)^{2/3}, \quad (4)$$

Table 2 The band gap, valence DOS effective mass (m_{dp}^* , m_e), conductive DOS effective mass (m_{dn}^* , m_e), valence band effective mass (m_{bp}^* , m_e), conductive band effective mass (m_{bn}^* , m_e) of the ordered ($\text{Ti}_4\text{Fe}_2\text{Ni}_2\text{Sb}_4$, $\text{V}_4\text{Fe}_2\text{Ni}_2\text{Ge}_4$) and SQS structures ($\text{Ti}_{16}\text{Fe}_8\text{Ni}_8\text{Sb}_{16}$, $\text{V}_{16}\text{Fe}_8\text{Ni}_8\text{Ge}_{16}$).

Candidates	E_g	m_{dp}^*	m_{dn}^*	m_{bp}^*	m_{bn}^*
$\text{Ti}_4\text{Fe}_2\text{Ni}_2\text{Sb}_4$	0.63	8.78	2.06	1.67	1.11
$\text{Ti}_{16}\text{Fe}_8\text{Ni}_8\text{Sb}_{16}$	0.44	6.86	2.91	2.44	2.71
$\text{V}_4\text{Fe}_2\text{Ni}_2\text{Ge}_4$	0.51	5.51	3.17	1.37	0.39
$\text{V}_{16}\text{Fe}_8\text{Ni}_8\text{Ge}_{16}$	0.38	3.21	2.51	1.25	0.55

where, $m_d^* = N_V^{2/3} m_b^*$ for N_V degenerate, equivalent bands. Based on the electronic structures, we have known that the band degeneracy of p-type $\text{Ti}_4\text{Fe}_2\text{Ni}_2\text{Sb}_4$ is large (effective $N_{vp} = 11$), and the corresponding p-type DOS effective mass is $m_{dp}^* = 8.78 m_e$. While its n-type counterpart has a light effective mass of $m_{dn}^* = 2.06 m_e$. This explains the higher p-type Seebeck coefficients of $\text{Ti}_4\text{Fe}_2\text{Ni}_2\text{Sb}_4$ (Fig. 5) at the same n . On the other hand, although the p-type SQS structure ($\text{Ti}_{16}\text{Fe}_8\text{Ni}_8\text{Sb}_{16}$) also has a large band degeneracy (effective $N_{vp} = 11$) and DOS effective mass ($m_{dp}^* = 6.86 m_e$). Its m_{dp}^* is still smaller than that of the ordered p-type $\text{Ti}_4\text{Fe}_2\text{Ni}_2\text{Sb}_4$. Thus, the ordered $\text{Ti}_4\text{Fe}_2\text{Ni}_2\text{Sb}_4$ structure exhibits a larger p-type Seebeck coefficient at the same carrier concentration (n). Similarly, for $\text{V}_4\text{Fe}_2\text{Ni}_2\text{Ge}_4$ and $\text{V}_{16}\text{Fe}_8\text{Ni}_8\text{Ge}_{16}$ (Fig. 5c and 5d), the large DOS effective masses in the ordered $\text{V}_4\text{Fe}_2\text{Ni}_2\text{Ge}_4$ ($m_{dp}^* = 5.51 m_e$, $m_{dn}^* = 3.17 m_e$) result both higher p- and n-type Seebeck coefficient than the SQS $\text{V}_{16}\text{Fe}_8\text{Ni}_8\text{Ge}_{16}$ ($m_{dp}^* = 3.21 m_e$, $m_{dn}^* = 2.51 m_e$) at the same n .

Electrical resistivity depends on the carrier mobility: $\rho = 1/ne\mu$, where μ is inversely proportional to the conductivity effective mass of a single band ($\mu \propto \tau_{ch}/m_b^*$)⁴⁹. As a consequence, lower electrical resistivity of the ordered $\text{Ti}_4\text{Fe}_2\text{Ni}_2\text{Sb}_4$ results from the small band effective masses ($m_{bp}^* = 1.67 m_e$, $m_{bn}^* = 1.11 m_e$) compared to those of the SQS $\text{Ti}_{16}\text{Fe}_8\text{Ni}_8\text{Sb}_{16}$ ($m_{bp}^* = 2.44 m_e$, $m_{bn}^* = 2.71 m_e$). Thus, the p- and n-type electrical resistivities of $\text{Ti}_4\text{Fe}_2\text{Ni}_2\text{Sb}_4$ are all lower compared to that of $\text{Ti}_{16}\text{Fe}_8\text{Ni}_8\text{Sb}_{16}$ because of the smaller band effective mass assuming the same τ_{ch} and n (The electronic thermal conductivities are shown in Fig. S4 in the Supplementary Information.).

Owing to the high Seebeck coefficients and lower electrical resistivities calculated here (assuming the same τ_{ch}), the ordered $\text{Ti}_4\text{Fe}_2\text{Ni}_2\text{Sb}_4$ and $\text{V}_4\text{Fe}_2\text{Ni}_2\text{Ge}_4$ structures possess higher p-type power factors (assuming the same n) (Fig. 5e and 5f) compared to the SQS structures. $\text{V}_4\text{Fe}_2\text{Ni}_2\text{Ge}_4$ is predicted to show similarly promising n-type thermoelectric properties. Therefore, ordered structures may be an effective way to achieve the excellent weighted mobility (Fig. S5 in Supplementary Information) in the double half-Heusler thermoelectric materials.

3.2.3 Thermal transport properties

To be promising thermoelectric materials, low lattice thermal conductivity is also needed. Recently, taking into account the Born-von-Karman periodic boundary conditions,^{50,51} the theoretical model can predict results that agrees with the calculated lattice

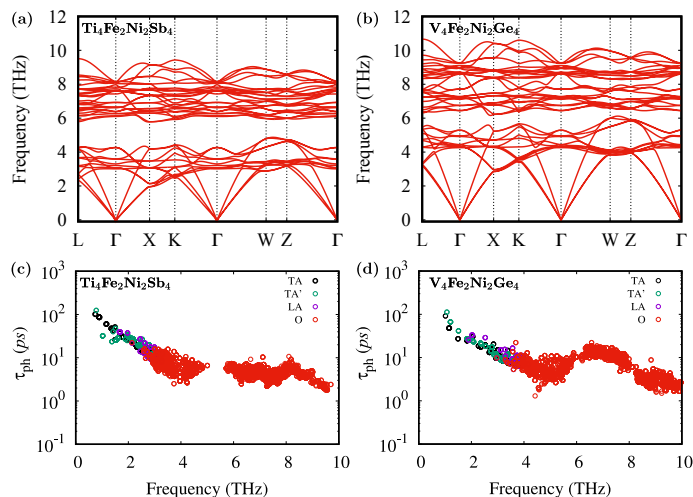


Fig. 6 The phonon dispersions and frequency-dependent phonon relaxation time of (a)(c) $\text{Ti}_4\text{Fe}_2\text{Ni}_2\text{Sb}_4$ and (b)(d) $\text{V}_4\text{Fe}_2\text{Ni}_2\text{Ge}_4$. TA, TA' and LA are the two transverse and one longitudinal acoustic branches. O represents the optical phonons.

thermal conductivity. Nevertheless, with the second-order harmonic and third-order anharmonic interatomic force constants, we calculate the thermal transport properties. The phonon spectrums of two ordered $\text{Ti}_4\text{Fe}_2\text{Ni}_2\text{Sb}_4$ and $\text{V}_4\text{Fe}_2\text{Ni}_2\text{Ge}_4$ structures (Fig. 6a and 6b) show no imaginary frequency throughout the Brillouin zone, indicating stability of the two ground state structures. It is worth noting that they all have some low-frequency optical modes mixed with the acoustic ones. Besides, the low-frequency optical branches of $\text{Ti}_4\text{Fe}_2\text{Ni}_2\text{Sb}_4$ are much lower than those of $\text{V}_4\text{Fe}_2\text{Ni}_2\text{Ge}_4$, indicating enhanced strong coupling to the acoustic modes.

Moreover, the low-laying optical band pushes the acoustic band frequencies lower, reducing phonon speed and therefore thermal conductivity. The maximum acoustic phonon frequencies of $\text{Ti}_4\text{Fe}_2\text{Ni}_2\text{Sb}_4$ and $\text{V}_4\text{Fe}_2\text{Ni}_2\text{Ge}_4$ are 3.28 and 4.16 THz, respectively. The lower frequencies of $\text{Ti}_4\text{Fe}_2\text{Ni}_2\text{Sb}_4$ suggest the softer sound velocities than the counterpart of $\text{V}_4\text{Fe}_2\text{Ni}_2\text{Ge}_4$. As shown in Table 3, the averaged phonon velocities of two transverse (TA, TA') and one longitudinal (LA) for $\text{Ti}_4\text{Fe}_2\text{Ni}_2\text{Sb}_4$ and $\text{V}_4\text{Fe}_2\text{Ni}_2\text{Ge}_4$ are 3937 and 4451 m/s, respectively. Thus, lower thermal conductivities of $\text{Ti}_4\text{Fe}_2\text{Ni}_2\text{Sb}_4$ are expected. The calculated three-phonon anharmonic scattering relaxation times are shown in Fig. 6 (c) and (d). $\text{Ti}_4\text{Fe}_2\text{Ni}_2\text{Sb}_4$ and $\text{V}_4\text{Fe}_2\text{Ni}_2\text{Ge}_4$ have similar phonon scattering relaxation times, suggesting similar anharmonicity. Therefore, the thermal conductivity difference of the two compounds would come from the different phonon velocities.

Table 3 The average transverse (TA/TA') and longitudinal (LA), Debye temperatures ($\Theta_{TA/TA'/LA}$) (K), phonon velocities ($v_{TA/TA'/LA}$) (m/s) of $\text{Ti}_4\text{Fe}_2\text{Ni}_2\text{Sb}_4$ and $\text{V}_4\text{Fe}_2\text{Ni}_2\text{Ge}_4$.

Candidates	Θ_{TA}	$\Theta_{TA'}$	Θ_{LA}	v_{TA}	$v_{TA'}$	v_{LA}
$\text{Ti}_4\text{Fe}_2\text{Ni}_2\text{Sb}_4$	152	153	157	2983	3288	5539
$\text{V}_4\text{Fe}_2\text{Ni}_2\text{Ge}_4$	189	190	200	3549	3603	6202

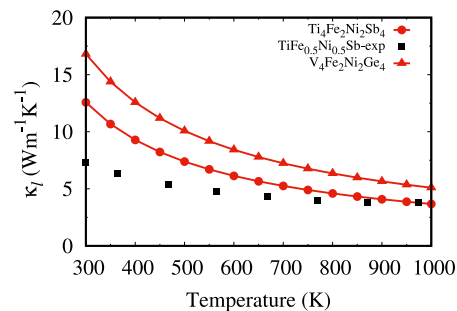


Fig. 7 Temperature dependent lattice thermal conductivity of ground states ($\text{Ti}_4\text{Fe}_2\text{Ni}_2\text{Sb}_4$, red line with circles, and $\text{V}_4\text{Fe}_2\text{Ni}_2\text{Ge}_4$, red line with triangles). The black squares are experimental data of $\text{TiFe}_{0.5}\text{Ni}_{0.5}\text{Sb}$ in Ref. [14].

Phonon dispersions largely affect the thermal transport properties. As is expected from the acoustic branches and similar phonon relaxation time (Fig. 6), the lattice thermal conductivity of $\text{Ti}_4\text{Fe}_2\text{Ni}_2\text{Sb}_4$ ($12.5 \text{ W m}^{-1} \text{ K}^{-1}$ at 300 K, Fig. 7) is lower than that of $\text{V}_4\text{Fe}_2\text{Ni}_2\text{Ge}_4$ ($16.6 \text{ W m}^{-1} \text{ K}^{-1}$ at 300 K), due to the lower phonon velocities. Comparing with the $\text{TiFe}_{1-x}\text{Ni}_x\text{Sb}$ solid solution, the ordered structure has a higher lattice thermal conductivity than the experimentally used solid solution $\text{TiFe}_{0.5}\text{Ni}_{0.5}\text{Sb}$ ($7.29 \text{ W m}^{-1} \text{ K}^{-1}$ at 300 K). With an increase in temperature, they gradually approach to the same value ($3.77 \text{ W m}^{-1} \text{ K}^{-1}$ at 974 K).

3.2.4 Thermoelectric performance

Owing to the high valley degeneracy, low conductivity mass and relatively low thermal conductivities, the p-/n-type zT values of ordered $\text{Ti}_4\text{Fe}_2\text{Ni}_2\text{Sb}_4$ structure (assuming a constant $\tau_{ch} = 10 \text{ fs}$ and carrier concentration of 10^{21} cm^{-3}) is 1.75 and 0.64 at 1000 K, which are higher than those in the experimentally measured solid solution cases (0.7 and 0.5 for p- and n-type)¹⁴. Similarly, $\text{V}_4\text{Fe}_2\text{Ni}_2\text{Ge}_4$ is predicted to have high p-type (1.33) and n-type (0.95) zT values as well (assuming a constant $\tau_{ch} = 10 \text{ fs}$ and carrier concentration of 10^{21} cm^{-3}). Therefore, the two ordered 17-19 electron structures are the promising thermoelectric candidates with environmentally friendly and earth-abundant elements. More importantly, forming ordered structures instead of the solid solutions is an effective way to achieve the excellent thermoelectric properties in the 17-19 electron HH designs.

4 Conclusions

Through density-functional theory combined with cluster expansion method, we have determined the $\text{TiFe}_{1-x}\text{Ni}_x\text{Sb}$, $\text{ZrFe}_{1-x}\text{Ni}_x\text{Bi}$ and $\text{VFe}_{1-x}\text{Ni}_x\text{Ge}$ pseudo-binary phase diagrams. We discovered two thermodynamically stable ground states of $\text{Ti}_4\text{Fe}_2\text{Ni}_2\text{Sb}_4$ and $\text{V}_4\text{Fe}_2\text{Ni}_2\text{Ge}_4$. Based on the electronic structures and electrical transport calculations, the ordered structures of $\text{Ti}_4\text{Fe}_2\text{Ni}_2\text{Sb}_4$ and $\text{V}_4\text{Fe}_2\text{Ni}_2\text{Ge}_4$ possess more promising p- and n-type electrical properties than the corresponding solid solutions owing to the heavier DOS but lighter band effective masses. Additionally, using the phonon Boltzmann transport equations, the thermal conductivities of the ordered structures are calculated to gradually approach to solid solution counterparts with increasing temperature, which we ascribe to the low-laying acoustic

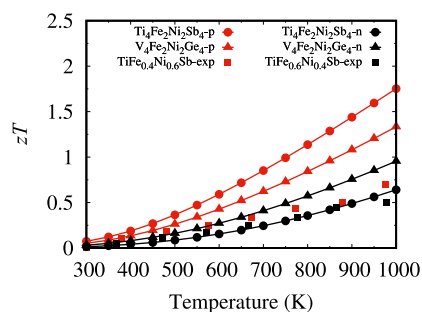


Fig. 8 Predicted zT values (at the same $\tau_{ch} = 10$ fs and carrier concentration of 10^{21} cm $^{-3}$) of $\text{Ti}_4\text{Fe}_2\text{Ni}_2\text{Sb}_4$ (lines with circles) and $\text{V}_4\text{Fe}_2\text{Ni}_2\text{Ge}_4$ (lines with triangles). The red and black lines represent the p- and n-type, respectively. The squares are experimental data of $\text{TiFe}_{0.4}\text{Ni}_{0.6}\text{Sb}$ and $\text{TiFe}_{0.6}\text{Ni}_{0.4}\text{Sb}$ in Ref. [14].

phonon branches. The predicted electrical and thermal properties, $\text{Ti}_4\text{Fe}_2\text{Ni}_2\text{Sb}_4$ and $\text{V}_4\text{Fe}_2\text{Ni}_2\text{Ge}_4$ combine to show high p-type zT values (1.75 and 1.33 at 1000 K) are possible. Our work suggests that forming ordered structures is an effective strategy to maintain the excellent electrical properties and relatively low thermal conductivities of HH compounds. Experimental methods to synthesize materials in the low-temperature ground states are strongly recommended.

Acknowledgements

Y. Z. acknowledges financial support from National Natural Science Foundation of China Grant Nos. 11774347. G. J. S. acknowledges support from the "Accelerated Discovery of Compositionally Complex Alloys for Direct Thermal Energy Conversion" award DE-AC02-76SF00515, and the U.S. Department of Energy, Office of Energy Efficiency and Renewable Energy (EERE). S. G. acknowledges support from the China Scholarship Council (CSC). The authors acknowledge helpful discussions with Shiqiang Hao at Northwestern University. The supercomputing services from Center for Computational Science of CASHIPS, the ScGrid of Supercomputing Center, Computer Network Information Center of Chinese Academy of Science and AM-HPC are gratefully acknowledged for high-performance computing.

References

- 1 L. E. Bell, *Science*, 2008, **321**, 1457–1461.
- 2 G. J. Snyder and E. S. Toberer, *Nat. Mater.*, 2008, **7**, 105–114.
- 3 J. He and T. M. Tritt, *Science*, 2017, **357**, year.
- 4 Y. Pei, H. Wang and G. J. Snyder, *Adv. Mater.*, 2012, **24**, 6125–6135.
- 5 G. J. Snyder, A. H. Snyder, M. Wood, R. Gurunathan, B. H. Snyder and C. Niu, *Adv. Mater.*, 2020, 2001537.
- 6 Z. Feng, Y. Fu, Y. Zhang and D. J. Singh, *Phys. Rev. B*, 2020, **101**, 064301.
- 7 Z. Feng, Y. Fu, A. Putatunda, Y. Zhang and D. J. Singh, *Phys. Rev. B*, 2019, **100**, 085202.
- 8 J. Carrete, W. Li, N. Mingo, S. Wang and S. Curtarolo, *Phys. Rev. X*, 2014, **4**, 011019.
- 9 W. G. Zeier, J. Schmitt, G. Hautier, U. Aydemir, Z. M. Gibbs,

- C. Felser and G. J. Snyder, *Nat. Rev. Mater.*, 2016, **1**, 16032.
- 10 T. Graf, C. Felser and S. S. Parkin, *Prog. Solid State Chem.*, 2011, **39**, 1–50.
- 11 S. Anand, K. Xia, V. I. Hegde, U. Aydemir, V. Kocovski, T. Zhu, C. Wolverton and G. J. Snyder, *Energy Environ. Sci.*, 2018, **11**, 1480–1488.
- 12 S. Anand, M. Wood, Y. Xia, C. Wolverton and G. J. Snyder, *Joule*, 2019, **3**, 1226–1238.
- 13 J. Toboła, L. Jodin, P. Pecheur, H. Scherrer, G. Venturini, B. Malaman and S. Kaprzyk, *Phys. Rev. B*, 2001, **64**, 155103.
- 14 Z. Liu, S. Guo, Y. Wu, J. Mao, Q. Zhu, H. Zhu, Y. Pei, J. Sui, Y. Zhang and Z. Ren, *Adv. Funct. Mater.*, 2019, **29**, 1905044.
- 15 M. T. Dylla, A. Dunn, S. Anand, A. Jain and G. J. Snyder, *Research*, 2020, **2020**, 6375171.
- 16 G. Li, Q. An, U. Aydemir, W. A. Goddard III, M. Wood, P. Zhai, Q. Zhang and G. J. Snyder, *J. Mater. Chem. A*, 2016, **4**, 14625–14636.
- 17 C. Fu, S. Bai, Y. Liu, Y. Tang, L. Chen, X. Zhao and T. Zhu, *Nat. Commun.*, 2015, **6**, 8144.
- 18 S. Guo, K. Yang, Z. Zeng and Y. Zhang, *Phys. Chem. Chem. Phys.*, 2018, **20**, 14441–14449.
- 19 H. Zhu, J. Mao, Y. Li, J. Sun, Y. Wang, Q. Zhu, G. Li, Q. Song, J. Zhou, Y. Fu, R. He, T. Tong, Z. Liu, W. Ren, L. You, Z. Wang, J. Luo, A. Sotnikov, J. Bao, K. Nielsch, G. Chen, S. D. J. and Z. Ren, *Nat. Commun.*, 2019, **10**, 270.
- 20 S. Guo, T. Jia and Y. Zhang, *J. Phys. Chem. C*, 2019, **123**, 18824–18833.
- 21 S. Bhattacharya and G. K. Madsen, *J. Mater. Chem. C*, 2016, **4**, 11261–11268.
- 22 Y. Zhang, E. Skoug, J. Cain, V. Ozoliņš, D. Morelli and C. Wolverton, *Phys. Rev. B*, 2012, **85**, 054306.
- 23 G. Kresse and D. Joubert, *Phys. Rev. B*, 1999, **59**, 1758.
- 24 J. P. Perdew, K. Burke and M. Ernzerhof, *Phys. Rev. Lett.*, 1996, **77**, 3865.
- 25 H. J. Monkhorst and J. D. Pack, *Phys. Rev. B*, 1976, **13**, 5188.
- 26 P. V. Medeiros, S. Stafström and J. Björk, *Phys. Rev. B*, 2014, **89**, 041407.
- 27 Y. Zhang, V. Blum and K. Reuter, *Phys. Rev. B*, 2007, **75**, 235406.
- 28 Y. Zhang, V. Ozoliņš, D. Morelli and C. Wolverton, *Chem. Mater.*, 2014, **26**, 3427–3435.
- 29 S. Hao, L.-D. Zhao, C.-Q. Chen, V. P. Dravid, M. G. Kanatzidis and C. M. Wolverton, *J. Am. Chem. Soc.*, 2014, **136**, 1628–1635.
- 30 A. Kohan, P. Tapesch, G. Ceder and C. Wolverton, *Comput. Mater. Sci.*, 1998, **9**, 389–396.
- 31 A. Van de Walle, P. Tiwary, M. De Jong, D. Olmsted, M. Asta, A. Dick, D. Shin, Y. Wang, L.-Q. Chen and Z.-K. Liu, *Calphad*, 2013, **42**, 13–18.
- 32 Y. Zhang, B. Feng, H. Hayashi, T. Tohei, I. Tanaka, Y. Ikuhara and H. Ohta, *J. Appl. Phys.*, 2017, **121**, 185102.
- 33 J. W. Doak, C. Wolverton and V. Ozoliņš, *Phys. Rev. B*, 2015, **92**, 174306.
- 34 A. Berche and P. Jund, *Intermetallics*, 2018, **92**, 62–71.

- 35 C. Wolverton, *Acta Mater.*, 2001, **49**, 3129–3142.
- 36 T. Jia, Z. Feng, S. Guo, X. Zhang and Y. Zhang, *ACS Appl. Mater. Interfaces*, 2020, **12**, 11852–11864.
- 37 G. K. Madsen and D. J. Singh, *Comput. Phys. Commun.*, 2006, **175**, 67–71.
- 38 G. K. Madsen, J. Carrete and M. J. Verstraete, *Computer Physics Communications*, 2018, **231**, 140–145.
- 39 J. Yang, H. Li, T. Wu, W. Zhang, L. Chen and J. Yang, *Adv. Funct. Mater.*, 2008, **18**, 2880–2888.
- 40 X. Gonze and C. Lee, *Phys. Rev. B*, 1997, **55**, 10355.
- 41 W. Li, J. Carrete, N. A. Katcho and N. Mingo, *Comput. Phys. Commun.*, 2014, **185**, 1747–1758.
- 42 J. Carrete, B. Vermeersch, A. Katre, A. van Roekeghem, T. Wang, G. K. Madsen and N. Mingo, *Comput. Phys. Commun.*, 2017, **220**, 351–362.
- 43 N. Naghibolashrafi, S. Keshavarz, V. I. Hegde, A. Gupta, W. Butler, J. Romero, K. Munira, P. LeClair, D. Mazumdar, J. Ma, A. W. Ghosh and C. Wolverton, *Phys. Rev. B*, 2016, **93**, 104424.
- 44 S. Anand, K. Xia, T. Zhu, C. Wolverton and G. J. Snyder, *Adv. Energy Mater.*, 2018, **8**, 1801409.
- 45 J. E. Saal, S. Kirklin, M. Aykol, B. Meredig and C. Wolverton, *JOM*, 2013, **65**, 1501–1509.
- 46 S. Kirklin, J. E. Saal, B. Meredig, A. Thompson, J. W. Doak, M. Aykol, S. Rühl and C. Wolverton, *npj Comput. Mater.*, 2015, **1**, 15010.
- 47 S. Guo, S. Anand, Y. Zhang and G. J. Snyder, *Chemistry of Materials*, 2020.
- 48 K. Xia, P. Nan, S. Tan, Y. Wang, B. Ge, W. Zhang, S. Anand, X. Zhao, G. J. Snyder and T. Zhu, *Energy & Environmental Science*, 2019, **12**, 1568–1574.
- 49 Z. M. Gibbs, F. Ricci, G. Li, H. Zhu, K. Persson, G. Ceder, G. Hautier, A. Jain and G. J. Snyder, *npj Comput. Mater.*, 2017, **3**, 1–7.
- 50 G. J. Snyder, M. T. Agne and R. Gurunathan, *National Science Review*, 2019, **6**, 380–381.
- 51 Z. Chen, X. Zhang, S. Lin, L. Chen and Y. Pei, *National Science Review*, 2018, **5**, 888–894.

TOC Image

